MNRAS 000, 1–?? (2016) Preprint 13 December 2016 Compiled using MNRAS LATEX style file v3.0

Observations of the γ-ray pulsar J1932+1916 in X-rays

A. Karpova[1⋆], P. Shternin[1], D. Zyuzin[1], A. Danilenko[1], Yu. Shibanov[1,2]
[1]Ioffe Institute, Politekhnicheskaya 26, St. Petersburg, 194021, Russia
[2]Peter the Great St. Petersburg Polytechnic University, Politekhnicheskaya 29, St. Petersburg, 195251, Russia

arXiv:1612.03647v1 [astro-ph.HE] 12 Dec 2016

Accepted XXX. Received YYY; in original form ZZZ

ABSTRACT

We present the analysis of the archival *Suzaku* and *Swift* X-ray observations of the young γ-ray pulsar J1932+1916 field. The data revealed a point-like object at the γ-ray position of the pulsar and diffuse X-ray emission around it. Spectra of the point-like source and diffuse emission are well-described by absorbed power-law models with spectral parameters typical for pulsar plus pulsar wind nebula systems. Therefore we suggest that *Suzaku* and *Swift* detected the X-ray counterpart of PSR J1932+1916. Assuming this interpretation, we constrain the distance to the pulsar in the range of 2–6 kpc. We also suggest possible association of the pulsar with the nearby supernova remnant G54.4−0.3 and discuss its implications for the pulsar proper motion, age and distance.

Key words: pulsars: general – pulsars: individual: PSR J1932+1916 – X-rays: stars

1 INTRODUCTION

The γ-ray pulsar PSR J1932+1916 (hereafter J1932) was recently discovered by Pletsch et al. (2013) in the *Fermi* Large Area Telescope data using a novel blind search algorithm initially dedicated for gravitational wave astronomy (Pletsch et al. 2012). Utilising the cloud computing with the Einstein@Home[1] volunteer-based supercomputing system, Pletsch et al. (2013) found four new young and energetic γ-ray pulsars. J1932 is the brightest and youngest of them. Subsequent radio observations failed to detect the pulsar (Pletsch et al. 2013). *Fermi* timing analysis yields the pulsar position R.A.=$19^{\rm h}32^{\rm m}19\overset{\rm s}{.}70(4)$ and Dec.=$+19^\circ16'39''(1)$[2] ($l = 54\overset{\circ}{.}7$ and $b = 0\overset{\circ}{.}08$). The pulsar has the characteristic age $\tau = 35$ kyr, the period $P = 208$ ms, the spin-down luminosity $\dot{E} = 4 \times 10^{35}$ erg s^{-1} and the magnetic field $B = 4.5 \times 10^{12}$ G. The so-called "pseudo-distance" estimate based on the empirical correlation between γ-ray fluxes and distances of pulsars (Abdo et al. 2013) results in the distance $D \sim 1.5$ kpc.

Relatively small distances and ages usually found for *Fermi* pulsars make these objects promising for X-ray studies. In the *Swift* X-ray Telescope (XRT) Point Source Catalogue (Evans et al. 2014), we found a source 1SXPS J193219.4+191635 which position agrees with the J1932 *Fermi* position allowing us to consider it as the pulsar X-ray counterpart candidate. Since there are only 9 source counts detected with XRT, one cannot make any definite conclusions on source properties. Fortunately, the J1932 field was also observed in 2010 with *Suzaku* as a part of follow-up X-ray observations of unidentified *Fermi* sources.

Here we report the analysis of the *Swift* and *Suzaku* observations. The observations and data reduction are described in Section 2. The *Suzaku* image creation procedure is presented in Section 3.1. We found an extended emission at the J1932 position in *Suzaku* images. We argue that the *Swift* point source is likely the pulsar J1932 counterpart, while the extended emission detected with *Suzaku* is the associated pulsar wind nebula (PWN). Its spatial structure and spectral properties are analysed in Sections 3.2 and 3.3. We discuss our results in Section 4 and summarise them in Section 5.

2 OBSERVATIONS AND DATA REDUCTION

2.1 *Swift* data

The J1932 field was observed with *Swift* three times. The possible X-ray counterpart 1SXPS J193219.4+191635 is detected only in the longest December 2010 observations (ObsID 00041803001, exposure $\approx$ 10 ks), still the detection significance is poor with the mean source count rate of $(1.3 \pm 0.6) \times 10^{-3}$ cts s^{-1}. Other observations are too shallow ($<$ 0.6 ks) and were ignored. We retrieved the reduced XRT data for the ObsID 00041803001 from the *Swift* archive. The respective image is shown in the top panel of Figure 1 where the source 1SXPS J193219.4+191635 is marked. Its astrometrically-corrected coordinates (Evans et al. 2014, Section 3.7) provided by the

⋆ E-mail: annakarpova1989@gmail.com
[1] http://einstein.phys.uwm.edu
[2] Numbers in parentheses are 1σ uncertainties corresponding to last significant digits quoted.

© 2016 The Authors

catalogue are R.A.=$19^{\rm h}32^{\rm m}19\overset{\rm s}{.}58$ and Dec.=$+19^\circ16'30\overset{''}{.}4$ with the position error circle radius of 7.2 arcsec (90 per cent confidence). The J1932 *Fermi* position lies within this error circle and is marked by the cross.

2.2 *Suzaku* data

The 45 ks *Suzaku* observations[3] of the J1932 field were carried out on 2010, April 27 and were pointed at R.A.=$293\overset{\circ}{.}04$ and Dec.=$19\overset{\circ}{.}26$. The *Suzaku* X-ray Telescope consisted of three front-illuminated X-ray Imaging Spectrometers (XIS0, XIS2 and XIS3) and one back-illuminated (XIS1), one of which, namely XIS2, was not operating since 2006 due to a damage event. In addition, a part of XIS0 chip was unavailable due to similar event occurred in 2009.[4]

For our analysis, we used the HEASOFT v.6.17 software. We reprocessed the unfiltered data using AEPIPELINE tool. We applied the standard screening criteria, i.e. we filtered flickering and hot pixels, time intervals corresponding to *Suzaku* passage of the South Atlantic Anomaly, the Earth elevation angles $<5^\circ$ and the Earth day-time elevation angles $<20^\circ$. Data of editing modes 3×3 and 5×5 were combined. After the procession, the effective exposure decreased down to about 24 ks. The decrease in exposure time is mainly due to the elevation angle constraints and the requirement of the instantaneous pointing to be within 1.5 arcmin of the mean.

3 DATA ANALYSIS

3.1 *Suzaku* Imaging

The images combined from two front-illuminated detectors XIS0 and XIS3 are shown in the middle panel of Figure 1 for the 2−8 keV band. The image in the 0.5–2 keV band from the back-illuminated detector XIS1 that provided higher sensitivity at lower energies is shown in the bottom panel of Figure 1. Constructing these images, we subtracted the non-X-ray background (NXB) generated via the XISNXBGEN task (Tawa et al. 2008). The resulting images were binned by 8 arcsec per pixel and smoothed with a Gaussian function of $\sigma = 4$ pixels width. The vignetting correction was then applied following the approach similar to one used by Fujinaga et al. (2013) and Izawa et al. (2015). This procedure requires a flat-field image construction on the basis of the appropriate astrophysical background (ABKG) spectral model.

For all XIS detectors, we extracted the ABKG spectra from the off-source polygon-shaped region shown in the middle panel of Figure 1. The detector responses were generated by the task XISRMFGEN and the Ancillary Response Files (ARFs) were generated by the task XISSIMARFGEN assuming a uniform sky source. Then the NXB-subtracted ABKG spectra from XIS 0–3 detectors were fitted simultaneously with XSPEC v.12.9.0 (Arnaud 1996). The employed spectral model consists of the Cosmic X-ray Background (CXB) and thermal plasma components. It is believed that CXB is isotropic but its contribution

[3] ObsID 405028010, PI T. Yasuyuki.
[4] http://www.astro.isas.ac.jp/suzaku/doc/suzakumemo/suzakumemo-2010-01.pdf

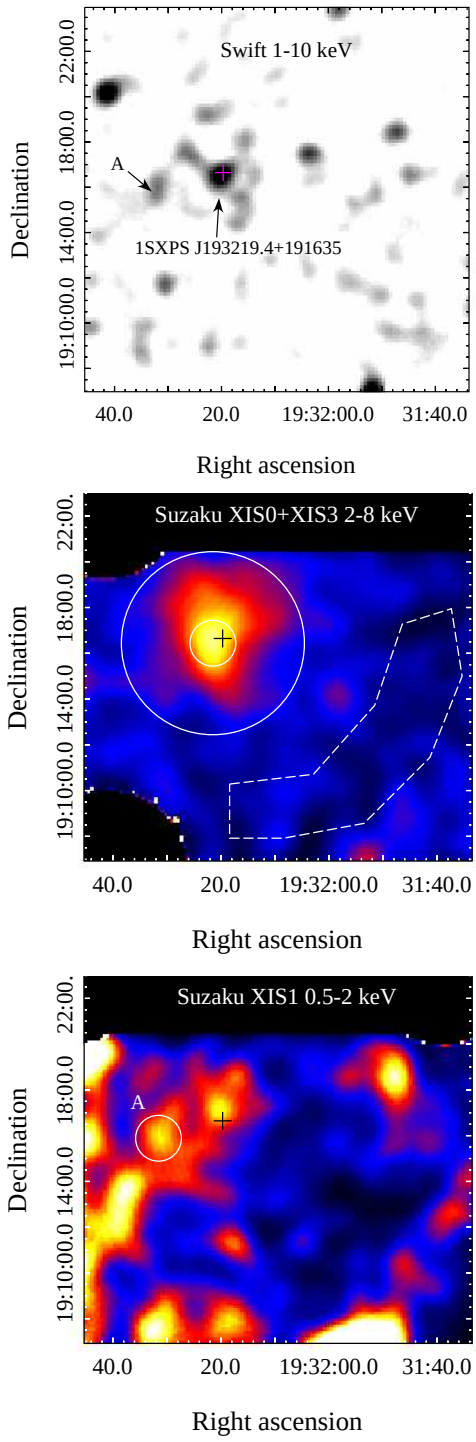

Figure 1. The PSR J1932+1916 field as observed with *Swift* XRT in 1–10 keV (top). The image is binned by 4 pixels and smoothed with a 5-pixel Gaussian kernel. The 1SXPS J193219.4+191635 source is marked. The 2–8 keV *Suzaku* XIS0+XIS3 (middle) and 0.5–2 keV XIS1 (bottom) images of the PSR J1932+1916 field. The images are binned by 8 pixels and smoothed with a Gaussian function of $\sigma = 4$ pixels. Linear brightness scale is used for the top and middle images and squared brightness scale is used for the bottom image. The *Fermi* position of PSR J1932+1916 (Pletsch et al. 2013) is shown by the crosses. In the middle panel, regions used for spectral analysis are shown (see text for details). The soft source 'A' falling in the extraction region is marked in the top and bottom panels.

for a particular line of sight depends on the total Galactic absorption for this direction. Thus, we fixed this component in the fit assuming the absorbed power-law spectrum with the photon index $\Gamma = 1.4$, the surface brightness $I = 5.4 \times 10^{-15}$ erg s^{-1} cm^{-2} arcmin^{-2} (in 2 − 10 keV band; Ueda et al. 1999) and the hydrogen column density $N_{\rm H} = 2.8 \times 10^{22}$ cm^{-2}. The latter value represents the total Galactic absorption in the J1932 direction and is discussed in detail in Section 4.1. The remaining part of the spectrum was fitted with the absorbed three-temperature optically thin thermal plasma model 3-T APEC. The best-fit parameters are given in Table 1. A lower number of components (e.g., 2-T model) resulted in statistically unacceptable fits. The primarily use of this model is to obtain a reliable approximation of the observed astrophysical background for the flat-field image construction and we do not justify its physical nature here. Finally, we simulated the flat field image with XISSIM tool (Ishisaki et al. 2007) using the best-fit spectral model for the background. The photon number in simulations was large enough to ensure the good statistics. This approach allowed us to correctly account for the vignetting in the extended source area.

3.2 Source extent

The resulting images demonstrate the presence of an X-ray excess spatially coincident with the *Fermi* position of J1932 (lower panels of Figure 1). However, the excess can not be described by the emission from a point source. This is illustrated in Figure 2 where we compare the radial brightness profile in the XIS0+XIS3 image extracted from the concentric annuli centred at the source brightness peak (crosses) with the radial profile of the *Suzaku* point spread function (PSF) shown with the black solid line. The latter is created with the xissim tool. It is clear that the X-ray emission extent is significantly larger than the PSF half-power diameter of 2 arcmin. Note that both NXB and ABKG are subtracted in Figure 2.

A relatively low spatial resolution of *Suzaku* does not allow to perform detailed morphological analysis of extended sources. However, an approximate spatial model of the source can be inferred. The model is useful to estimate the source extent and is necessary to obtain ARFs for the spectral analysis. For these purposes, we constructed NXB-subtracted images from XIS0 and XIS3 data in the 2–8 keV band. This band was chosen to eliminate the contribution from a soft point-like source 'A' clearly seen in the *Swift* and XIS1 images of Figure 1. This source is listed as 1SXPS J193231.7+191540 in the 1SXPS catalogue. The ABKG images generated as discussed in the previous section were subtracted. The images were then binned and smoothed in the same way as before. The resulting images were fitted with the CIAO v.4.7 SHERPA software using simulated PSF images as convolution kernels. We found that the spatial brightness distribution of the considered source can be described with the model consisting of two 2D-Gaussian functions with negligible ellipticities: a broad one with the full width at half maximum (FWHM) $\approx$ 4.5 arcmin and a narrow one with FWHM $\lesssim$ 0.5 arcmin. Their centres are shifted by about 70 arcsec relative to each other. In Figure 2, the radial profiles of the best-fit model and its two components convolved with the PSF are shown with green solid, dashed and dotted lines,

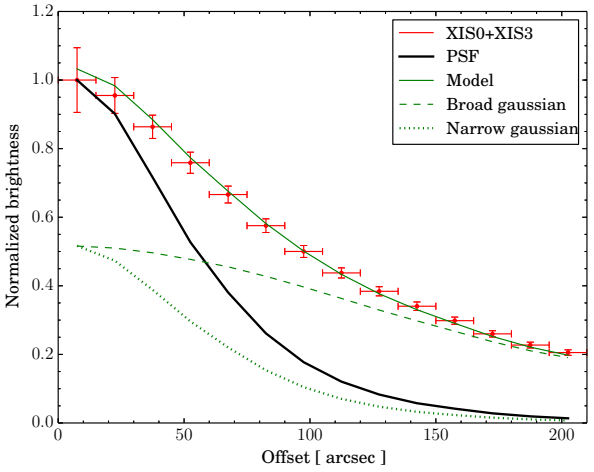

Figure 2. Comparison of the observed radial brightness profile (crosses) of the *Suzaku* J1932 counterpart candidate with the simulated PSF (black solid line) and the best-fit spatial model (green solid line). Narrow and broad Gaussian model components are shown with dotted and dashed lines, respectively, see text for details.

respectively. The broad emission component can be interpreted as the PWN powered by J1932. The narrow component peak position offsets by about 30 arcsec from the point-like *Swift* counterpart candidate position. The offset significance is only about 1.5σ taking into account the 90 per cent XIS positional uncertainties of 19 arcsec (Uchiyama et al. 2008) and the 7.2 arcsec *Swift* position error. It is thus natural to assume that the narrow component represents the pulsar itself. On the other hand, it may just be a bright compact feature of the PWN. Better spatial resolution observations are necessary to verify that.

3.3 X-ray spectral analysis

We assume that the X-ray emission around the J1932 position has contributions from the point-like pulsar presumably detected with *Swift* and from the extended source seen with *Suzaku*. In what follows, we call the point-like component as 'PSR' and the extended component as 'PWN'. According to the analysis in Section 3.2, the PSR component must contribute to the central part of the extended source in *Suzaku* data. Bearing this in mind, we divided the extended source region in two parts shown in the bottom-left panel of Figure 1: the central 60 arcsec-radius circle and the ring with radii of 60 arcsec and 4 arcmin. In the latter region, the 60 arcsec-radius circle containing the point-like source 'A' was excluded from the spectral analysis. The *Suzaku* spectra were extracted from these two regions from all XIS detectors. NXB spectra appropriate for each region were generated with XISNXBGEN for each detector and subtracted.

We simultaneously fitted all 9 (3 regions × 3 XIS detectors) *Suzaku* spectra assuming the PSR, PWN and ABKG contributions in the central circle and in the ring and the ABKG contribution in the polygon region. Using XISSIMARFGEN tool, for each detector we constructed seven ARFs for each contribution. For the PWN component, we generated ARFs adopting the broad Gaussian spatial model with

σ =4.5 arcmin as derived in the previous section. The narrow Gaussian was not included since we attributed it to the pulsar. On the other hand, as noted in Section 3.2, it may represent the PWN compact structure. However, we checked that the addition of this narrow Gaussian in ARFs generation for the PWN does not affect final results significantly. For the PSR component, we generated point-source ARFs. Finally, for all regions, we generated ARFs for an uniformly extended source to be used with the ABKG component.

In order to put constrains on the point-source contribution which follow from the *Swift* observations, we also included *Swift* data in the spectral analysis. We extracted spectrum from the 30 arcsec-radius aperture centred at the 1SXPS J193219.4+191635 position and background was extracted from the source-free region in the *Swift* image.

The ABKG model was already described above in Sect 3.1. For the PSR and the PWN components, we used the absorbed power-law (PL) models with shared values of the hydrogen absorption column density. To account for the photoelectric absorption we used the PHABS model with default cross-sections BCMC (Balucinska-Church & McCammon 1992) and abundances ANGR (Anders & Grevesse 1989). The parameters for the PSR model were tied between the *Swift* and *Suzaku* spectra. Different contributions from the PWN to different *Suzaku* spectra are automatically taken into account by the ARFs. In principle, some contribution from the PWN emission to the *Swift* source spectrum can be expected. Basing on the spatial model of Section 3.2, we found that $\approx$ 4 per cent of the total PWN flux contribute to the *Swift* extraction aperture. This was included in the spectral analysis. Using XRTMKARF tool, we generated two XRT ARFs: for the extended emission to account for the possible PWN contribution and for the point source PSR.

We used the unbinned spectra to fit for the model parameters. The XSPEC software was applied to calculate the likelihood statistics. *C*-statistics (Cash 1979) was used for the *Swift* spectra, while the PGSTAT[5] statistics was used for the *Suzaku* spectra. The latter statistics corresponds to a Poisson source with a Gaussian background and is appropriate since the XISNXBGEN task returns the simulated NXB count rate with Gaussian error-bars. Spectra were fitted in the 0.5–10 keV range. At higher energies, the *Suzaku* spectra are dominated by NXB. The estimation of the parameter uncertainties was performed via the Bayesian inference framework. We sampled the posterior parameter space using the Markov chain Monte-Carlo (MCMC) procedure. Specifically, we used the affine-invariant MCMC sampler (Goodman & Weare 2010) employed as a convenient python package EMCEE by Foreman-Mackey et al. (2013). Best-fit parameters and the 90 per cent uncertainties are presented in Table 1. The latter were estimated as the 90 per cent highest posterior density intervals of the corresponding marginal posterior density distributions.

The goodness of the fit is illustrated in Figure 3 where the spectra from the polygon (top panel), the ring (middle panel) and the central circle (bottom panel) regions are compared with the best-fit spectral models. For illustration purposes, the polygon and circle spectra are binned to ensure 30 counts in each energy bin, and the ring region spectra are binned to ensure 10 counts per energy bin. We also show the corresponding χ^2 values in each plot. As seen from Figure 3, the model describes the observed data reasonably well. We do not see any significant unmodelled features in the residuals. The excess in the residuals at energies >7 keV for the XIS1 spectra is due to incomplete NXB modelling at high energies (see, e.g., Izawa et al. 2015). We also assessed the goodness of fit for our model by calculating the posterior predictive p-value (e.g., Gelman et al. 2003) for the the Pearson χ^2 test statistics (PCHI in XSPEC) appropriate for the Poisson data. We used XSPEC FAKEIT tool to generate N=256 synthetic spectra for the model parameters sampled from the posterior distributions. We found that only in 68 per cent of simulations, the test statistics value for the synthetic data was smaller than for the observed data. This means that our model cannot be rejected.

Table 1. Best-fit parameters for the ABKG, the presumed PWN and the PSR. All errors are at 90 per cent confidence.

ABKG	
$N_{\rm H_1}^a$, 10^{22} cm^{-2}	$0.8^{+0.3}_{-0.3}$
T_1^b, keV	$0.06^{+0.02}_{-0.01}$
N_1^c, 100 cm^{-5}	$0.6^{+38}_{-0.5}$
$N_{\rm H_2}$, 10^{22} cm^{-2}	$1.0^{+0.2}_{-0.2}$
T_2^b, keV	$0.5^{+0.1}_{-0.2}$
N_2^c, 10^{-2} cm^{-5}	2^{+2}_{-1}
$N_{\rm H_3}$, 10^{22} cm^{-2}	$1.8^{+1.0}_{-0.7}$
T_3^b, keV	$1.9^{+1.1}_{-0.5}$
N_3^c, 10^{-3} cm^{-5}	11^{+4}_{-5}
PWN	
$N_{\rm H}^a$, 10^{22} cm^{-2}	$1.2^{+0.3}_{-0.3}$
Γ^d	$1.8^{+0.4}_{-0.3}$
N_{PL}^e, 10^{-4} photons s^{-1} cm^{-2} keV^{-1}	$2.6^{+1.5}_{-1.0}$
f_X^f, 10^{-12} erg s^{-1} cm^{-2}	$1.2^{+0.3}_{-0.2}$
PSR	
Γ^d	$1.4^{+1.0}_{-1.0}$
N_{PL}^e, 10^{-5} photons s^{-1} cm^{-2} keV^{-1}	$1.7^{+4.6}_{-1.3}$
f_X^f, 10^{-13} erg s^{-1} cm^{-2}	$1.3^{+0.9}_{-0.5}$

[a] Hydrogen column density; for the PSR it is the same as for the PWN
[b] Plasma temperature
[c] APEC normalization
[d] Photon index
[e] PL normalization
[f] Unabsorbed flux in the 0.5–8 keV band

4 DISCUSSION

We found that the spectrum of the extended source detected with *Suzaku* at the γ-ray position of the pulsar J1932 is well

[5] https://heasarc.gsfc.nasa.gov/xanadu/xspec/manual/XSappendixStatistics.html

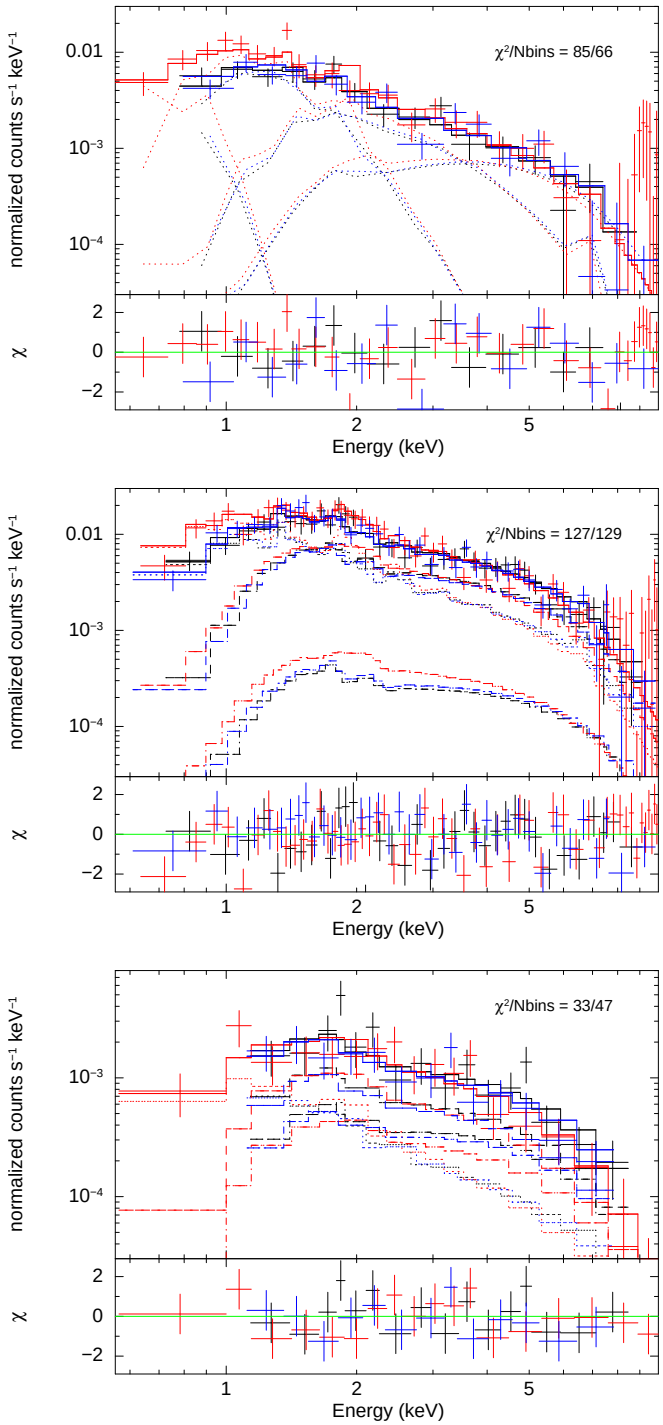

Figure 3. Observed spectra (crosses) and best fit models (solid lines) extracted from the polygon (top panel), the ring (middle panel) and the central circle (bottom panel) regions shown in Figure 1. XIS0, XIS1 and XIS3 data are presented by black, red and blue colours, respectively. Low sub-panels demonstrate fit residuals normalised by the data uncertainties in each spectral bin (χ). In the top and middle panels, the spectra are binned for illustrative purposes by 30 counts per bin, while in the bottom panels – by 10 counts per bin. Dotted lines in the top panel represent four ABKG model components. In the middle and bottom panels, dotted, dashed and dot-dashed lines represent the ABKG, the PWN and the PSR contributions, respectively. The total χ^2 values and the numbers of energy bins (Nbins) are shown in top sub-panels for each spectral extraction region.

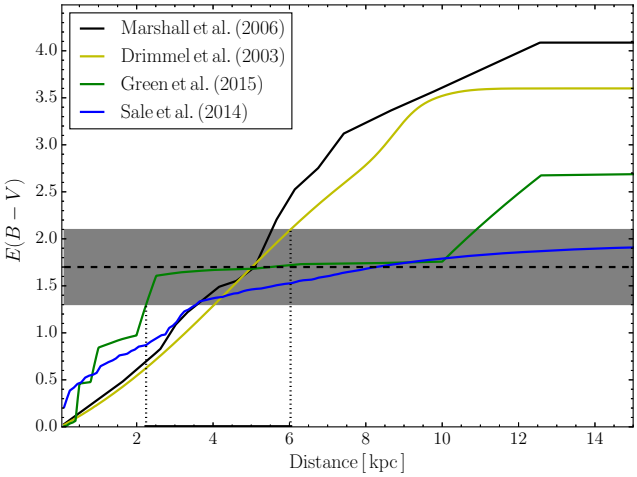

Figure 4. Extinction–distance relations in the J1932 direction according to various extinction maps. The grey-filled horizontal strip corresponds to the J1932 extinction value inferred from the X-ray spectral fit. The adopted distance range is between the vertical dotted lines, see text for details.

described by an absorbed power law model with $\Gamma \approx 2$. This value is typical for PWNe (Kargaltsev & Pavlov 2008). $N_{\rm H}$ value obtained from the spectral fits is twice lower than the total Galactic $N_{\rm H}$ in this direction excluding an extragalactic interpretation. The pulsar itself is not directly identified with *Suzaku* but is likely visible with *Swift* as a point-like source. Its spectrum can be described by the absorbed power-law, although the PL parameters are poorly constrained, i.e., $\Gamma \approx 0.5 - 2.5$. Nevertheless, the values obtained are not unreasonable neither for pulsars nor for compact PWNe. It is instructive to transform the obtained X-ray fluxes into luminosities and to compare them with the data on other young PSR+PWN systems. To do this, the reliable distance estimate is required.

4.1 Distance to J1932

Due to the absence of J1932 in the radio, the only available distance estimate $D \sim 1.5$ kpc was obtained by Pletsch et al. (2013) using the empirical correlation between the γ-ray flux and the distance, although this estimate is known to be very crude (e.g., Abdo et al. 2013). Assuming 100 per cent efficiency in γ-rays, Pletsch et al. (2013) estimated upper limit of 6.6 kpc, neglecting, however, possible beaming of the emission. If the γ-ray emission is highly beamed, the distance can be even higher.

Another possible way to estimate the distance is based on the analysis of the interstellar extinction towards the source. Existing 3D extinction maps of the Galaxy mainly trace the dust absorption quantified by the selective extinction value $E(B-V)$. The latter can be estimated using an empirical correlation between $E(B-V)$ and $N_{\rm H}$. Here we use the relation $N_{\rm H} = (0.7 \pm 0.1) \times E(B-V) \times 10^{22}$ cm^{-2} given by Watson (2011) basing on the analysis of the gamma-ray bursts. This relation is consistent with one given by Güver & Özel (2009) constructed using the optical and X-

ray observations of supernova remnants (SNRs).[6] With this relation in hand, the total Galactic $N_{\rm H}$ can be readily obtained from the total $E(B-V)$ value. The total selective extinction in the J1932 direction according to the Galactic Dust Reddening and Extinction Service[7] is $E(B-V) \approx 4$ (Schlafly & Finkbeiner 2011), transforming to the total $N_{\rm H} \approx 2.8 \times 10^{22}$ cm^{-2}. We thus use this value in the CXB spectral model in Sections 3.1–3.3.

Our X-ray spectral fits yield $N_{\rm H} = (1.2 \pm 0.3) \times 10^{22}$ cm^{-2} (Table 1) which transforms to $E(B-V) = 1.7 \pm 0.4$ (1σ errors). In Figure 4, we compare this range (grey-filled strip) with several extinction-distance relations for the J1932 direction constructed using the PYTHON package MWDUST (Bovy et al. 2016). The plot includes the extinction maps of Marshall et al. (2006, based on the reg-giant stars photometry in the 2MASS survey), Green et al. (2015, based on the main sequence star photometry in the Pan-STARRS and the 2MASS surveys), Sale et al. (2014, based on the INT/WFC Photometric Hα Survey) and Drimmel, Cabrera-Lavers & López-Corredoira (2003, based on an analytic model fit to the COBE DIRBE data). The maps of Sale et al. (2014) and Green et al. (2015) are not applicable at distances $\gtrsim 5$ kpc in this direction due to paucity of the main-sequence stars in the surveys. On the other hand, Marshall et al. (2006) map is based on brighter reg giant stars and reliably traces the extinctions to larger distances. According to Figure 4, it also agrees well with the map of Drimmel et al. (2003). However, at smaller distances ($\lesssim 2$ kpc), the map of Green et al. (2015) is preferable for the similar reason: there are much more main sequence stars than red giants.

Therefore, we base our conservative lower limit of the distance estimate on the Green et al. (2015) map and the upper limit on the Drimmel et al. (2003) map. This results in the J1932 distance range of 2−6 kpc (bounded by vertical dotted lines in Figure 4). For convenience, below we use the notation $D_{4\rm kpc} \equiv D/(4\ {\rm kpc})$.

4.2 Luminosity, efficiency and PWN size

Estimated X-ray luminosities of J1932 and its PWN are $L_{\rm PSR} = 2.5^{+1.7}_{-1.0} \times 10^{32} D_{4\rm kpc}$ erg s^{-1} and $L_{\rm PWN} = 2.3^{+0.6}_{-0.4} \times 10^{33} D_{4\rm kpc}$ erg s^{-1}. To compare them with the luminosities of other pulsar+PWN systems, we used the data from Kargaltsev & Pavlov (2008) with updates from Shibanov et al. (2016). The plots of the pulsar and PWN luminosities versus the spin-down luminosity are presented in Figure 5 where J1932 is shown by the red triangle. As seen, if the detected X-ray sources are indeed related to J1932, this pulsar produces a brighter PWN in comparison to other ones with similar $\dot{E}$. However, this system is generally compatible with the overall $L-\dot{E}$ pulsar and PWN distributions. The ratio $L_{\rm PWN}/L_{\rm PSR} \approx 10$ for J1932 is also consistent with the range $0.1 \lesssim L_{\rm PWN}/L_{\rm PSR} \lesssim 10$ obtained by Kargaltsev & Pavlov (2008) using the current sample of these systems. This supports the pulsar and PWN identification of the detected sources.

For J1932, the γ-ray flux is about 8×10^{-11} erg s^{-1} cm^{-1} in the 0.1–100 GeV range (Pletsch et al. 2013). Thus, the pulsar γ-ray to X-ray flux ratio is ~ 600 that is typical for γ-ray pulsars with similar $\dot{E}$ (Abdo et al. 2013).

Bamba et al. (2010) pointed on a correlation between PWNe X-ray physical sizes and pulsar characteristic ages. Accounting for the distance uncertainties, the J1932 PWN size (defined as three times the Gaussian σ, Bamba et al. 2010) is 6.5 ± 3.5 pc. For the J1932 characteristic age of 35 kyr, the obtained size agrees well with the reported correlation (Bamba et al. 2010).

4.3 Association with the supernova remnant G54.4−0.3

J1932 is located near the edge of the supernova remnant (SNR) G54.4−0.3. The radio image of the remnant from the VLA Galactic Plane Survey (Stil et al. 2006) is shown in Figure 6. In the radio, it is a shell-type SNR with a nearly circular shape and angular diameter of ~ 40 arcmin (Junkes, Fuerst & Reich 1992). Using the *ROSAT* observations of the remnant, Junkes (1996) estimated the absorbing column density in its direction of about 10^{22} cm^{-2}. This value is comparable to our $N_{\rm H}$ estimate for J1932 pointing to the similar distances and allowing us to assume that J1932 is associated with G54.4−0.3.

In this case, independent distance constraints are possible. Based on CO observations, Junkes et al. (1992) associated G54.4−0.3 with a molecular cloud at the velocity in the local standard of rest (LSR) $v_{\rm LSR} = 40$ km s^{-1}. This led to the kinematic distance of 3.0 ± 0.8 kpc (near-side) or 7.0 ± 0.8 kpc (far-side) using the Galaxy rotation curve of Burton (1988). Park et al. (2013) revisited this value using rotational curves of Brand & Blitz (1993) and Levine, Heiles & Blitz (2008) and obtained 3.1 kpc and 3.9 kpc, respectively, for the near side of the rotational curve. Finally they adopted the distance of 3.3 kpc given by Case & Bhattacharya (1998). The modern rotation curve from Reid et al. (2009)[8] gives $D = 4.7 \pm 1.5$ kpc (near-side) and $D = 5.0 \pm 1.5$ kpc (far-side). Finally, the Bayesian distance estimator (Reid et al. 2016)[9], which assumes spiral arm associations, provides $D = 4.0 \pm 0.4$ kpc placing the SNR into the Local Spur. This distance is also supported by the presence of an OB association around G54.4−0.3 at the distances of 3−4 kpc (Junkes et al. 1992).

All this is compatible with our distance estimates for J1932. Note, that it is natural to associate J1932 with the OB association. Even if the pulsar is not related to G54.4−0.3, its progenitor star was likely the member of this association.

Using the Inner-Galaxy Arecibo *L*-band Feed Array HI survey, Park et al. (2013) found an expansion of the G54.4−0.3 shell. The measured expansion velocity allowed them to estimate the dynamical age of the SNR $t_{\rm dyn} \approx 95$ kyr (for $D = 3.3$ kpc). This is by a factor of 2.7 larger

[6] We rely on the work of Güver & Özel (2009) instead of their more recent work Foight et al. (2016) since Güver & Özel (2009) use the same abundances from Anders & Grevesse (1989) as we do, while Foight et al. (2016) use abundances from Wilms, Allen & McCray (2000).

[7] https://irsa.ipac.caltech.edu/applications/DUST/

[8] http://bessel.vlbi-astrometry.org/revised_kd

[9] http://bessel.vlbi-astrometry.org/bayesian

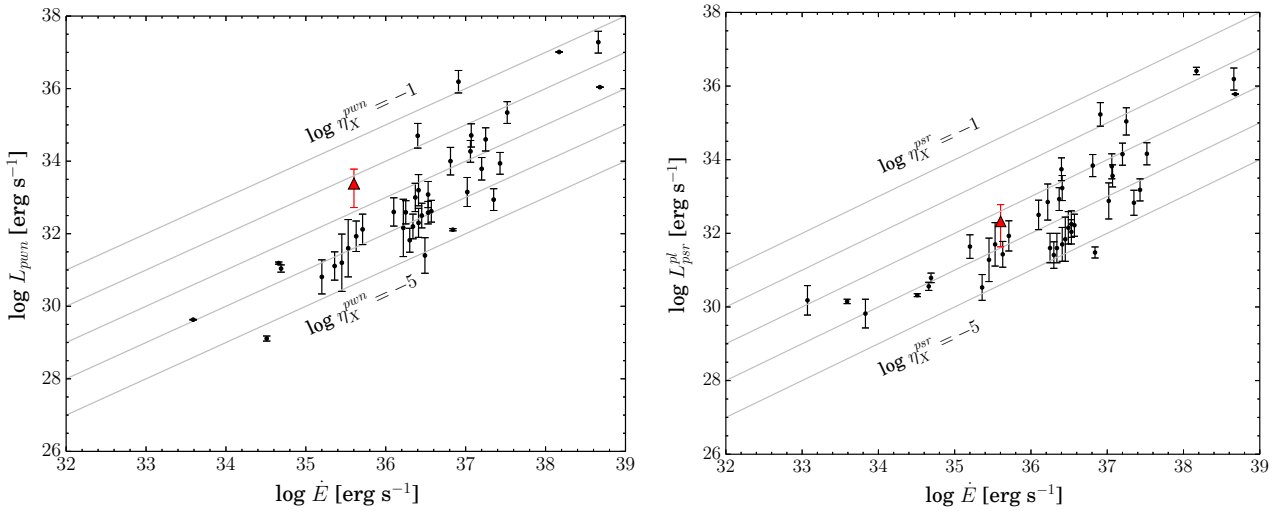

Figure 5. PWN luminosities (*left*) and PSR luminosities (*right*) versus spin-down energies for various objects. The J1932 luminosities are shown by triangles for $D = 4$ kpc. Error bars combine the 1σ flux uncertainties and the distance range uncertainty.

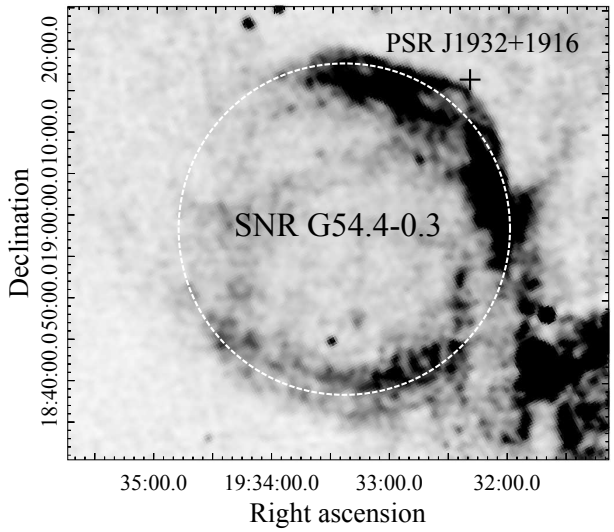

Figure 6. Image of the SNR G54.4−0.3 obtained from the VLA Galactic Plane Survey (VGPS). The *Fermi* position of J1932 is marked by the cross. The dashed circle shows the SNR shape.

than the characteristic age of J1932. One can consider this as a counter-argument for the association, however there are examples where pulsar spin-down ages are considerably smaller than associated SNR ages (e.g., Lin & Zhang 2006).

The most natural way to check the reality of this association is to measure the pulsar proper motion. In case of the association, it should be about $34\tau_{35}^{-1}$ mas yr^{-1}, where τ_{35} is J1932 age in units of 35 kyr. Then the pulsar tangential velocity is $\approx 650 D_{4\rm kpc}\tau_{35}^{-1}$ km s^{-1}, compatible with the empirical transverse velocity distribution for young pulsars (Hobbs et al. 2005). If the proper motion vector points to the centre of the remnant, it will be a strong argument in favour of the association. Even if the proper motion is not detected, it will be possible to estimate its direction basing on the PWN morphology. For the PSR travelling sufficiently fast, one expects a bow-shock morphology with a long trail (e.g., Gaensler & Slane 2006).

5 CONCLUSIONS

We analysed the archival *Swift* and *Suzaku* X-ray observations of the radio-quiet gamma-ray pulsar J1932+1916 field. At the pulsar position, *Swift* found the point-like X-ray source, while *Suzaku* revealed diffuse emission with extent of about 5 arcmin (FWHM). The spectral properties of these sources are compatible with those of PSR+PWN systems suggesting the pulsar nature of the detected emission.

The analysis of the interstellar extinction allowed us to constrain the distance to the pulsar within the range of $2 - 6$ kpc. At this distance, the observed PWN candidate appears somewhat more luminous than PWNe powered by pulsars with similar $\dot{E}$ while the candidate PSR luminosity is in line with the values for other pulsars.

It is possible that J1932 is associated with the SNR G54.4−0.3 located at $D \sim 3-4$ kpc. This association is supported by comparable values of the interstellar extinctions towards J1932 and the SNR. If the presumable association is true, the prominent proper motion of the pulsar can be expected.

Future observations with better spatial resolution are necessary to confirm J1932 counterpart nature of the X-ray source by deeper studies of its morphology and spectral properties.

ACKNOWLEDGMENTS

We thank Dmitrii Barsukov, Serge Balashev and Aida Kirichenko for discussions. The work was supported by the Russian Science Foundation, grant 14-12-00316. For Figure 6 we used the data from the VGPS survey conducted by the National Radio Astronomy Observatory (NRAO) instruments. NRAO is a facility of the National Science Foun-

dation operated under cooperative agreement by Associated Universities, Inc.

REFERENCES

Abdo A. A., et al., 2013, ApJS, 208, 17
Anders E., Grevesse N., 1989, Geochimica Cosmochimica Acta, 53, 197
Arnaud K. A., 1996, in Jacoby G. H., Barnes J., eds, Astronomical Society of the Pacific Conference Series Vol. 101, Astronomical Data Analysis Software and Systems V. p. 17
Balucinska-Church M., McCammon D., 1992, ApJ, 400, 699
Bamba A., Anada T., Dotani T., Mori K., Yamazaki R., Ebisawa K., Vink J., 2010, ApJ, 719, L116
Bovy J., Rix H.-W., Green G. M., Schlafly E. F., Finkbeiner D. P., 2016, ApJ, 818, 130
Brand J., Blitz L., 1993, A&A, 275, 67
Case G. L., Bhattacharya D., 1998, ApJ, 504, 761
Cash W., 1979, ApJ, 228, 939
Drimmel R., Cabrera-Lavers A., López-Corredoira M., 2003, A&A, 409, 205
Evans P. A., et al., 2014, ApJS, 210, 8
Foight D. R., Güver T., Özel F., Slane P. O., 2016, ApJ, 826, 66
Foreman-Mackey D., Hogg D. W., Lang D., Goodman J., 2013, PASP, 125, 306
Fujinaga T., et al., 2013, PASJ, 65, 61
Gaensler B. M., Slane P. O., 2006, ARA&A, 44, 17
Gelman A., Carlin J. B., Stern H. S., Rubin D. B., 2003, Bayesian Data Analysis, 2 edn. Texts in Statistical Science, Chapman & Hall/CRC, Boca Raton, London, New York, Washington, D.C.
Goodman J., Weare J., 2010, Comm. App. Math. Comp. Sci., 5, 65
Green G. M., et al., 2015, ApJ, 810, 25
Güver T., Özel F., 2009, MNRAS, 400, 2050
Hobbs G., Lorimer D. R., Lyne A. G., Kramer M., 2005, MNRAS, 360, 974
Ishisaki Y., et al., 2007, PASJ, 59, 113
Izawa M., Dotani T., Fujinaga T., Bamba A., Ozaki M., Hiraga J. S., 2015, PASJ, 67, 43
Junkes N., 1996, in Blitz L., Teuben P. J., eds, IAU Symposium Vol. 169, Unsolved Problems of the Milky Way. Kluwer, Dordrecht, p. 627
Junkes N., Fuerst E., Reich W., 1992, A&AS, 96, 1
Kargaltsev O., Pavlov G. G., 2008, in Bassa C., Wang Z., Cumming A., Kaspi V. M., eds, American Institute of Physics Conference Series Vol. 983, 40 Years of Pulsars: Millisecond Pulsars, Magnetars and More. Melville, New-York, pp 171–185 (arXiv:0801.2602), doi:10.1063/1.2900138
Levine E. S., Heiles C., Blitz L., 2008, ApJ, 679, 1288
Lin J. R., Zhang S. N., 2006, in Lowry J. A., ed., Trends in Pulsar Research. p. 79
Marshall D. J., Robin A. C., Reylé C., Schultheis M., Picaud S., 2006, A&A, 453, 635
Park G., et al., 2013, ApJ, 777, 14
Pletsch H. J., et al., 2012, ApJ, 744, 105
Pletsch H. J., et al., 2013, ApJ, 779, L11
Reid M. J., et al., 2009, ApJ, 700, 137
Reid M. J., Dame T. M., Menten K. M., Brunthaler A., 2016, ApJ, 823, 77
Sale S. E., et al., 2014, MNRAS, 443, 2907
Schlafly E. F., Finkbeiner D. P., 2011, ApJ, 737, 103
Shibanov Y., Danilenko A., Zharikov S., Shternin P., Zyuzin D., 2016, preprint, (arXiv:1608.03005)
Stil J. M., et al., 2006, AJ, 132, 1158
Tawa N., et al., 2008, PASJ, 60, 11
Uchiyama Y., et al., 2008, PASJ, 60, S35
Ueda Y., et al., 1999, ApJ, 518, 656
Watson D., 2011, A&A, 533, A16
Wilms J., Allen A., McCray R., 2000, ApJ, 542, 914